UNIVERSITÀ DI PARMA

ARCHIVIO DELLA RICERCA

University of Parma Research Repository

Thermal characterization of a multi-turn pulsating heat pipe in microgravity conditions: Statistical approach to the local wall-to-fluid heat flux

note finali coverpage

(Article begins on next page)

22 December 2024

Thermal characterization of a multi-turn PHP in microgravity conditions: statistical approach to the local wall-to-fluid heat flux

Luca Pagliarini[a], Luca Cattani[b*], Fabio Bozzoli[a,d], Mauro Mameli[f], Sauro Filippeschi[f], Sara Rainieri[a,c], Marco Marengo[e]

[a] Department of Engineering and Architecture, University of Parma, Parco Area delle Scienze 181/A, Parma, Italy
[b] CIDEA Interdepartmental Centre, University of Parma, Parco Area delle Scienze 181/A, Parma, Italy
[c] European Space Agency – ESTEC, Noordwijk-ZH | The Netherlands
[d] SITEIA.PARMA Interdepartmental Centre, University of Parma, Parco Area delle Scienze 181/A, Parma, Italy
[e] School of Computing, Engineering and Mathematics, University of Brighton, Lewes Road, BN2 4GJ Brighton, UK
[f] Department of Energy, Systems Land and Construction Engineering, University of Pisa, Largo L. Lazzarino, Pisa, Italy

E-mail address of the corresponding Author (Luca Cattani): luca.cattani1@unipr.it

Abstract. A Pulsating Heat Pipe (PHP), specifically designed to be hosted on board the Heat Transfer Host of the International Space Station, is tested in microgravity conditions during the 67th Parabolic Flight Campaign promoted by the European Space Agency. The device consists in an aluminium tube (inner/outer diameter = 3/5 mm) closed in a 14 turns loop, half filled with FC-72. The PHP external wall temperature distribution are measured within the adiabatic section by means of a high-speed infrared camera. The resulting thermographic images are used as input data for the solution of the Inverse Heat Conduction Problem (IHCP) in the channels wall to estimate local time-space heat fluxes exchanged at the wall-fluid interface. The adopted post-processing method represents one of the first attempts to estimate the local wall-to-fluid heat flux in PHPs under microgravity conditions. A comprehensive investigation of the wall-to-fluid heat fluxes is performed on the overall device by means of an original statistical approach in order to study the PHP working regimes. The results highlight that such approach is capable of providing similar information regarding the fluid motion inside the PHP to those obtained by the traditional intrusive experimental methods (e.g. direct fluid temperature-pressure measurements) or transparent inserts (e.g. sapphire tube), which perturb the original layout of the PHP and require a complex experimental set-up.

Key words: Pulsating Heat Pipe, Microgravity Conditions, Inverse Heat Conduction Problem, Infrared Thermography.

1. Introduction

Pulsating Heat Pipes (PHPs) are two-phase heat transfer devices that achieved resounding interest in the last decades mainly thanks to their ability of working without any external source of electrical energy, coupled with their high heat transfer capability, great adaptability to many different layouts and low manufacturing cost [1]. In addition, PHPs can work in absence of gravity, thus making the investigation on such devices of primary importance also in the aerospace engineering field [2]. PHPs are often characterized in terms of global performance by evaluating their equivalent thermal resistance [3]. However, the full understanding of the working principles underlying the PHPs operation requires a more detailed insight into the complex local heat transfer phenomena occurring between the wall and the working fluid, not only regarding the analysis of a single channel, but also in the whole device. In the literature, different methodologies for characterizing the local thermal behaviour in two-phase flows have been proposed. Kim et al. [4] suggested a non-intrusive infrared (IR) technique for the evaluation of the heat flux exchanged between a multilayer wall and a two-phase flow with high spatial resolution, where both the outer and the inner surfaces were coated with a black opaque paint. Due to the multilayer absorption, emission and reflection of the thermal energy, the internal wall temperature was obtained by solving a conduction/radiation problem. The local heat transfer coefficient was additionally evaluated. Scammell et al. [5] adopted a similar approach for the evaluation of the heat flux and the local heat transfer coefficient exchanged by a Taylor bubble passing through a tube, internally and externally coated with a polyimide tape. Farahani and Karami [6] proposed a different technique for the evaluation of the heat flux exchanged between the working fluid and a boiling surface, consisting in wall

temperature measurements by means of thermocouples, therefore processed by means of an inverse problem resolution approach (conjugated gradient method).

The above-mentioned methods were similarly employed for the local heat transfer quantities evaluation in PHPs, i.e. the local wall-to-fluid heat flux and heat transfer coefficient. Specifically, Mameli et al. [7] estimated the local heat transfer coefficient in the evaporator zone of a two-turns PHP by measuring both the inner wall and the fluid temperature in the evaporator section of a Closed-loop Pulsating Heat Pipe (CLPHP) by means of thermocouples. Jo et al. [8] replicated the estimation procedure of [4] in the study of a five-turn closed-loop flat micro PHP, where both direct fluid visualisation and IR measurements of the wall-fluid interface temperature were achieved for the first time on the whole device. The presence of liquid slugs or vapour plugs in the flow pattern was assessed by thermography, and the local wall-to-fluid heat flux variations over time and along space between the liquid and vapour phases were reported. Moreover, a synchronization of the IR and the optical camera acquisitions allowed to define the areas in which the liquid/vapour phase was present, and the contribution of sensible/latent heat transfer in the overall PHP was estimated over time. However, the adopted multilayer wall can be hardly implemented from a manufacturing point of view on other kinds of PHPs, i.e. complex tubular PHPs. Cattani et al. [9] proposed a novel IR technique for the evaluation of time-space heat flux distributions in a single-loop PHP. In particular, the external wall of a sapphire channel, which is almost transparent to the mid-wave radiations ($\tau > 0.9$), was half coated with a high-emissivity opaque paint, thus providing simultaneous measurements of the external wall and fluid temperature. The local heat flux exchanged between the channel wall and the fluid within the adiabatic section of the device was evaluated by solving the Inverse Heat Conduction Problem (IHCP) in the wall. The results, successfully compared with the thermographic measurements of the fluid temperature, highlighted that the wall-to-fluid heat flux distributions in time can be adopted as reference for the flow motion assessment. In fact, during fluid oscillations and flow reversal phenomena, the wall-to-fluid heat flux provided information about the flow direction, although the fluid motion assessment is usually achieved by means of either intrusive techniques, i.e. temperature-pressure transducers directly inserted in the fluid flow and transparent inserts [10,11,12], or by using transparent PHPs for the direct fluid visualisation [13,14,15]. The effectiveness of the non-intrusive IR measurements for the fluid motion assessment was also pointed out by Karthikeyan et al. [16], who studied a multi-turn PHP for different heat load to the evaporator without any direct fluid visualisation, even though no local heat flux was here estimated.

The present work proposes to extend the IR analysis and the IHCP resolution approach presented in [9] to the thermal characterization of a multi-turn CLPHP, tested during the 67th Parabolic Flight Campaign (PFC) promoted by the European Space Agency (ESA), and already studied in terms of both evaporator/condenser wall temperature and fluid temperature/pressure fluctuations [12,17]. The proposed estimation technique aims at quantifying the local and instantaneous heat fluxes exchanged within the whole adiabatic section of the device, thus giving a deeper insight into the PHP working regimes for different heat loads by means of a post-processing procedure of this massive amount of data with an original statistical approach. To the authors' knowledge, such investigation represents one of the first attempts of detecting the flow motion characteristics on the whole adiabatic zone by means of the non-intrusive IR technique. The results are furthermore quantitatively compared with those obtained by the elaboration of fluid pressure signals, previously carried out in the same test conditions [17], to investigate the agreement between the non-intrusive IR technique and the intrusive measurements of the fluid pressure

2. Experimental facilities and image processing procedure

The studied device (Fig. 1) is made of an annealed aluminium tube (6060 alloy, I/O diameter = 3/5 mm), bent in 14 turns; the resulting staggered 3-D closed loop configuration (overall size: 220x80x25) is designed to fit the limiting constrains of the Heat Transfer Host aboard the International Space Station. It is essentially constituted by 3 sections, including the evaporator, condenser and adiabatic section. Two aluminium heat spreaders (100x12x10 mm) are brazed on the tube in the evaporator zone, holding two ceramic Ohmic heaters (Innovacera®, electrical resistance 18 $\Omega \pm 10$). The heating power is provided by a programmable power supply (GW-Instek®, PSH-6006A). The condenser zone is embedded between two aluminium heat spreaders (80x120x10 mm), cooled down by means of a Peltier cell system (8 Peltier cells by Adaptive Thermal Management®, ETH-127-14-11-S; control system by Meertstetter Engineering®, TEC 1123) coupled with a cold plate temperature control system loop (Aavid Thermalloy®). The temperature of the evaporator is measured through five T-type thermocouples located between the evaporator spreader and the heater while the

temperature at the condenser is monitored by six T-type thermocouples located between the Peltier cold side and the condenser aluminium heat spreader and two placed on the condenser heat spreader. All the thermocouples were calibrated with a thermal chamber (BINDER®) and a reference four wire Pt-100 (ITS-90 standard, max. error 0.035 K).
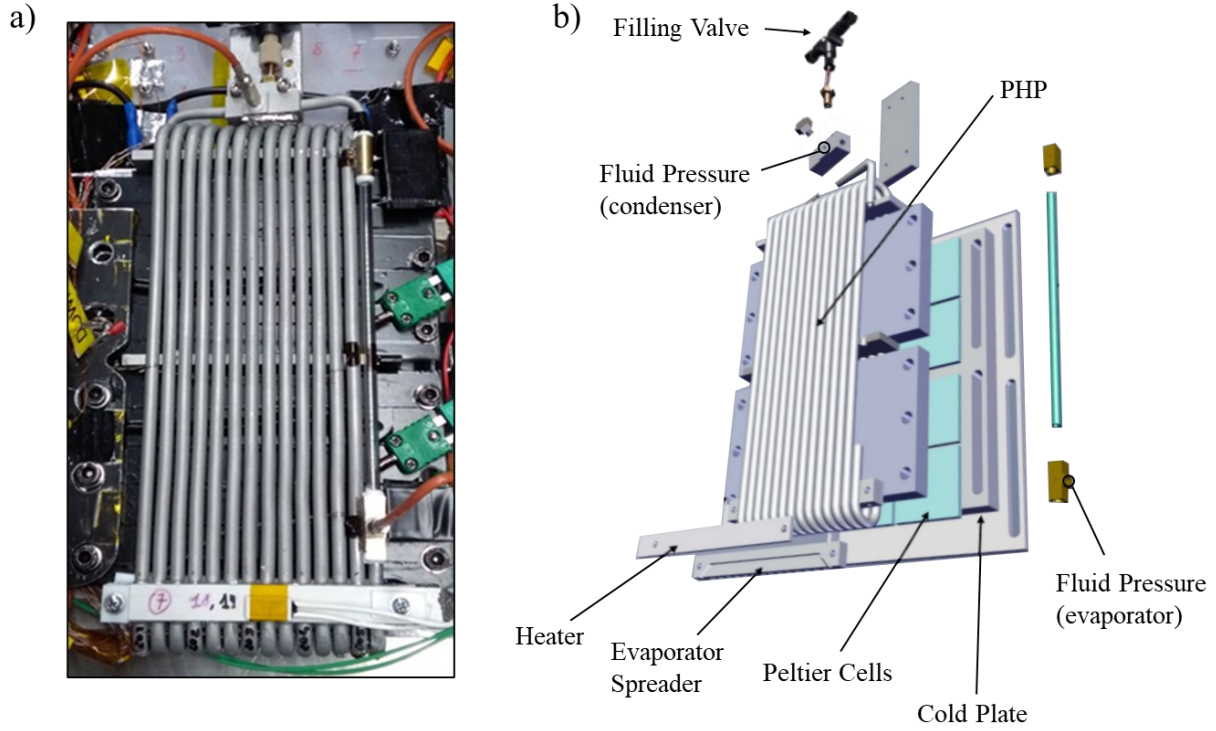

Figure 1: Overhead view of the device (a) and exploded 3D view (b).

The fluid pressure at the condenser and evaporator sections were measured by two miniature pressure transducers (Keller® PAA-M5-HB, 1 bar abs, 0.2% FSO accuracy). The thermocouples signals were recorded at 50 Hz, while the pressure measurements were sampled with a frequency of 200 Hz.

A sapphire insert is present in the adiabatic section in order to directly inspect the flow regimes and measure the fluid temperature distribution, as explained in the previous works [12,17]. The aluminium channels within the adiabatic section were uniformly coated with a high-emissivity opaque paint ($\varepsilon = 0,92$) and the temperature was acquired by means of a previously calibrated [18] high-speed and high-resolution infrared (IR) camera (AIM® TEC-MMG from ESA/ESTEC, 50 Hz, 1280x1024 pixels). The IR measurements were carried out in between the evaporator and the condenser since the adiabatic section was the only portion directly accessible to the IR camera. Specifically, the camera framed just a portion of the PHP adiabatic section (0.084 m long), highlighted with a green box in Fig. 2.

Since the IR measurements are reliable when the viewing angle is less than 30°, the analysis was carried out on 10 of the 14 PHP, numbered in Fig. 2. The uncertainty related to each measured parameter is listed in Table 1.

The device was first vacuumed (down to 10^{-6} mbar) and then partially filled by means of a micro-metering valve (IDEX® Upchurch Sc. P- 447), shown in Fig. 1b, with degassed FC-72 (filling ratio = $50 \pm 1\%$ vol.)

The test rig was then mounted on an Airbus A310 and a total of 93 parabolic trajectories were performed over three days. Every parabola provided about 20 seconds of microgravity conditions between two intervals of about 20 seconds of hyper-gravity each. The gravity level was monitored by accelerometers (sampling frequency = 10 Hz) attached to the floor structure of the aircraft. The device was oriented in bottom heated mode and tests were performed varying the heating power from 30 W up to 210 W. Each power input to the evaporator was provided before the microgravity period, thus maintaining the heat load constant for the whole parabolic trajectory.
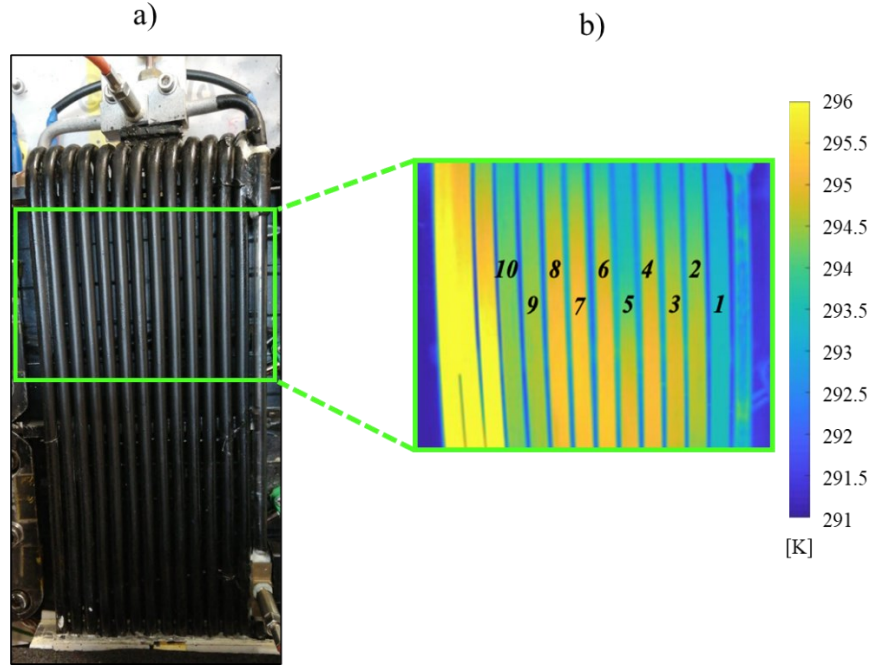
Figure 2: Framed PHP section (a) and representative thermographic image (b); the study was carried out focusing on 10 of the 14 PHP channels, considering a portion of 0.084 m.

Table 1: uncertanty of the measurement tools.

Parameter	Specs	Sampling frequency	Max error
Channel wall temperature	T-type Thermocouple (0.5 mm bead diameter)	50 Hz	± 0.1°C
	High-speed Medium Wave Infrared Camera	50 Hz	± 0.2°C
Fluid temperature	Omega® KMTSS-IM025E-150 K-Type thermocouple (0.25 mm bead diameter)	50 Hz	± 0.2°C
Fluid pressure	Keller® PAA-M5-HB, 1 bar abs	200 Hz	± 500 Pa
Power Input	GW-Instek®, PSH-6006A	-	± 3 W

3. Heat flux estimation procedure

Starting from the temperature distribution of the channels outer surface, acquired by means of the IR camera, the local convective heat flux at the fluid-internal wall interface was evaluated by solving the inverse heat conduction problem at the PHP wall. The test section, represented by each channel shown in Fig. 2, was modelled as a 2D-axisimmetric solid domain, sketched in Fig. 3, assuming that the temperature gradient is almost negligible along the circumferential coordinate.
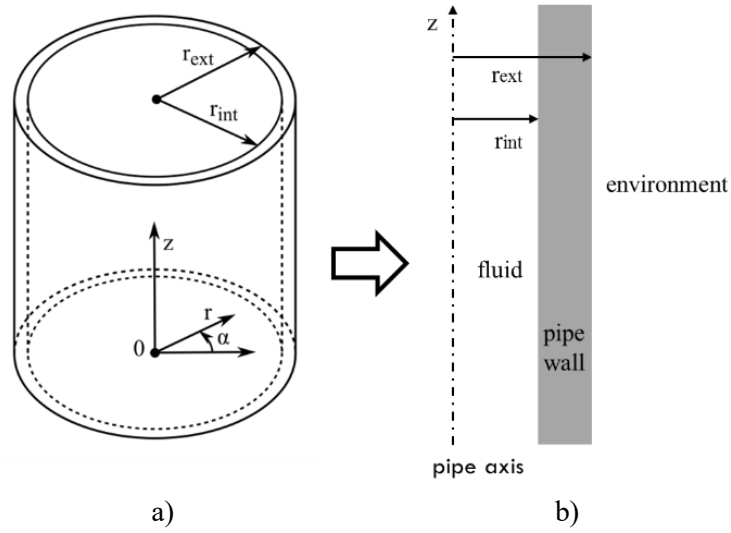
Figure 3: Sketch of the test section (a) and resulting 2D-axisimmetric domain (b), obtained by assuming the temperature gradient almost negligible along α.

The energy balance equation in the solid domain is expressed as follows [19]:

$$k\nabla^2 T = \rho c_p \frac{\partial T}{\partial t} \tag{1}$$

where k, ρ and c_p are the channel thermal conductivity, density and specific heat, respectively. The boundary conditions of Eq. (2a) and Eq. (2b), applied on the inner surface and on the outer surface of the channel, respectively, complete the energy balance equation:

$$k\frac{\partial T}{\partial r}\bigg|_{r=r_{int}} = q \tag{2a}$$

$$\frac{\partial T}{\partial r}\bigg|_{r=r_{ext}} = -\frac{(T - T_{env})}{R_{env}} \tag{2b}$$

The thermal conductivity k of the aluminium channel was certified by the manufacturer to be equal to 201 W/mK at 300 K and the overall heat-transfer resistance R_{env} between the channel wall and the surrounding environment was assumed equal to 0.1 m²K/W, which is a representative value for air natural convection with radiative heat transfer towards the environment. By assuming the thin-wall approximation, the temperature on the external surface was considered equal to that on the internal surface:

$$T(r,z) \cong T(r_{int}, z) \cong T(r_{ext}, z)) \tag{3}$$

Finally, the starting 3D domain was simplified as a 1D solid domain; the wall temperature is thus assumed to vary only along the axial coordinate z and time. With reference to the infinitesimal wall section of length Δz, described in Fig. 4b, the local energy balance equation assumes the form of Eq. (4).

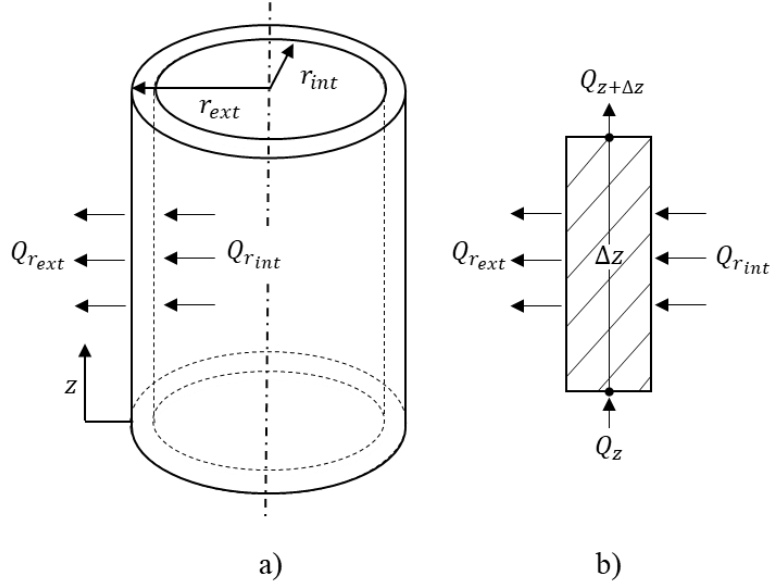$$Q_t = Q_z - Q_{z+dz} + Q_{r_{int}} - Q_{r_{ext}} \tag{4}$$

Figure 4: Portion of the test section (a) and generic wall element (b).

The thermal power terms are expressed as:

$$Q_z = -k \frac{\partial T}{\partial z} \cdot \pi(r_{ext}^2 - r_{int}^2) \tag{5a}$$

$$Q_{z+dz} = -k \frac{\partial T}{\partial z} \cdot \pi(r_{ext}^2 - r_{int}^2) - k \frac{\partial^2 T}{\partial z^2} \cdot \pi(r_{ext}^2 - r_{int}^2) \cdot \Delta z \tag{5b}$$

$$Q_t = \rho c_p \frac{\partial T}{\partial t} \cdot \pi(r_{ext}^2 - r_{int}^2) \cdot \Delta z \tag{5c}$$

$$Q_{r_{ext}} = \frac{(T - T_{env})}{R_{env}} \cdot 2\pi r_{ext} \cdot \Delta z \tag{5d}$$

$$Q_{r_{int}} = q \cdot 2\pi r_{int} \cdot \Delta z \tag{5e}$$

By substituting Eqs. (5a-5e) into Eq. (4), the energy equation becomes:

$$\rho c_p \frac{\partial T}{\partial t} \cdot \pi(r_{ext}^2 - r_{int}^2) = k \frac{\partial^2 T}{\partial z^2} \cdot \pi(r_{ext}^2 - r_{int}^2) + q \cdot 2\pi r_{int} - \frac{(T - T_{env})}{R_{env}} \cdot 2\pi r_{ext} \tag{6}$$

Finally, the heat flux on the wall inner surface results:

$$q = \frac{\left(\rho c_p \frac{\partial T}{\partial t} - k \frac{\partial^2 T}{\partial z^2}\right) \cdot (r_{ext}^2 - r_{int}^2) + \frac{(T - T_{env})}{R_{env}} \cdot 2r_{ext}}{2r_{int}} \tag{7}$$

During the tests, T_{env} varied in the range of 18÷20°C. Eq. (7) could be solved by means of the finite difference method:

$$q(z,t) = \frac{\left(\rho c_p \frac{T(z, t + \Delta t) - T(z, \Delta t)}{\Delta t} - k \frac{T(z + \Delta z, t) + T(z - \Delta z, t) - 2T(z, t)}{(\Delta z)^2}\right) \cdot (r_{ext}^2 - r_{int}^2) + \frac{(T(z, t) - T_{env})}{R_{env}} \cdot 2r_{ext}}{2r_{int}} \tag{8}$$

However, being experimental temperature data unavoidably noisy, Eq. (8) gives unstable results because the derivative operators are very sensitive to small perturbations in the input data when coupled with the destructive effect of noise [20]. A convenient way to overcome these difficulties is filtering out the unwanted noise from the raw temperature data. The effectiveness of the Gaussian kernel in this kind of approach was experimented by Murio et al. [21], Delpueyo et al. [22] and Bozzoli et al. [23]. The application of a Gaussian filter reduces the data high-frequency components, thus behaving alike the regularization term in the Tikhonov regularization method [20].

According to the filtering approach, the heat flux on the inner wall surface is evaluated as follows:

$$q(z,t) = \frac{\left(\rho c_p \frac{T_f(z,t+\Delta t) - T_f(z,\Delta t)}{\Delta t} - k \frac{T_f(z+\Delta z,t) + T_f(z-\Delta z,t) - 2T_f(z,t)}{(\Delta z)^2}\right) \cdot (r_{ext}{}^2 - r_{int}{}^2) + \frac{(T_f(z,t) - T_{env})}{R_{env}} \cdot 2r_{ext}}{2r_{int}} \quad (9)$$

where T_f is the filtered measured temperature. In particular, for wall temperature samples discretized into M spatial steps Δz and N time increments Δt, the Discrete Fourier Transform of the measured M×N temperature distribution T results in:

$$\mathcal{F}(T) = \tilde{T}(u,v) = \sum_{g=0}^{M-1} \sum_{h=0}^{N-1} T(g,h) e^{-j2\pi \frac{ug}{M}} e^{-j2\pi \frac{vh}{N}} \quad (10)$$

where u and v are the spatial and time coordinates in the frequency domain. By adopting the Gaussian filter, according to its 2D formulation, the Discrete Fourier transform of the filtered temperature becomes:

$$\mathcal{F}(T_f) = \tilde{T}_f(u,v) = H(u,v) \cdot \tilde{T}(u,v) \quad (11)$$

$H(u,v)$ is the transfer function for the Gaussian filter, defined as:

$$H(u,v) = e^{-(u^2+v^2)/2u_c^2} \quad (12)$$

where u_c is the cut-off frequency. Last, the Fourier image is converted back to the time-space domain:

$$\mathcal{F}^{-1}(\tilde{T}_f) = T_f(m,n) = \frac{1}{M \cdot N} \sum_{k=0}^{M-1} \sum_{l=0}^{N-1} \tilde{T}_f(k,l) e^{j2\pi \frac{km}{M}} e^{j2\pi \frac{ln}{N}} \quad (13)$$

Since in real applications the optimal cut-off frequency value is not known a priori, a criterion for such regularization parameter must be selected to successfully employ the regularization procedure. In the present analysis, the criterion provided by the discrepancy principle, originally formulated by Morozov [24], was adopted. According to this principle, the inverse problem solution is regarded to be sufficiently accurate when the difference between the measured T and filtered T_f temperatures is close to the standard deviation of the raw measurements. The cut-off frequency was then determined as the frequency at which the following condition was satisfied:

$$\frac{\left\| T_f - T \right\|_2^2}{N \cdot M} \cong \sigma_Y \quad (14)$$

where $\left\| \ \right\|_2$ stands for the 2-norm, N·M is the size of the matrix T and σ_Y is the standard deviation of the raw data, estimated by measuring the wall temperature distribution while maintaining the system under isothermal conditions. For the present study case, σ_Y was found to be equal to 0.06 K.

4. Validation of the estimation procedure

To validate the procedure presented in Section 3, synthetic temperature data were generated by solving the direct problem with a known distribution of the heat flux $q(z, t)$ at the internal wall surface. The numerical model for the direct problem was implemented within the Comsol Multiphysics® environment.

The resulting temperature distributions were then spoiled by Gaussian noise levels, characterized by a standard deviation σ ranging from 0.01 to 0.1 K, and used as input data for the Inverse Heat Conduction Problem (IHCP) solution approach. According to the expected results in the real cases, the convective heat flux q was assumed as a sinusoidal function characterized by time-space variations, where L is the length of the considered channel portion:

$$q(z, t) = A \cdot \cos{(p\pi t)} \cdot (1 + \frac{z}{8} \cdot L) \tag{16}$$

The effectiveness of the proposed approach at different heat flux amplitudes and frequencies was quantified by taking A equal to 2000 and 4000 W/m^2, while the p parameter was varied among 1.2, 1.6, 2 and 2.4, corresponding to frequencies of 0.6, 0.8, 1 and 1.2 Hz, respectively. The adopted values of amplitude and frequency are representative of the oscillatory phenomena that characterise the studied device [9,17].

From the direct problem, solved by using the wall-to-fluid heat fluxes of Eq. (16), the maximum residual between the internal and external wall temperatures was found to be about equal to 0.02 K. The thin-wall approximation of Eq. (3) is thus validated since the maximum residual is much lower than the noise level assumed in Section 3 for the experimental setup (0.06 K). It has to be underlined that the inverse approach in transient conditions is affected by the thermal inertia of the PHP channels that makes difficult to catch high-frequency phenomena. The effects of the aluminium wall on the wall-to-fluid heat flux restoration were thus studied by solving the direct problem, using heat fluxes of Eq. (16) with p ranging from 2.5 to 8 and A equal to 2000 W/m^2. For oscillation frequencies of the wall-to-fluid heat flux greater than 3 Hz ($p = 6$), the maximum variation of the external wall temperature was found to be lower than the noise level of the experimental setup. Hence, in this case, the thermographic measurements on the tube outer surface are able to catch transient phenomena that occur inside the PHP tube in a time higher than 0.3 s, while every other significantly faster transient phenomenon cannot be fully perceived on the outer surface due to the filtering effect of the aluminium wall.

To quantify the efficiency of the applied approach at different signal-to-noise levels, an error analysis was performed by evaluating the estimation error, defined as follows:

$$E_q = \frac{\|q_{restored} - q_{exact}\|_2}{A\sqrt{M \cdot N}} \tag{17}$$

In Fig. 5, the estimation error, evaluated for every combination of heat flux frequency and amplitude, is plotted against the noise level. For A equal to 4000 W/m^2, the estimation procedure is able to restore the heat flux distribution with good accuracy ($7\% < E_q < 20\%$), while, for $A = 2000 \ W/m^2$, the heat flux restoration procedure is affected by higher though acceptable restoration errors ($8\% < E_q < 25\%$). Moreover, the estimation error was observed to increase with the oscillation frequency. For noise level equal to 0.06 K (experimental setup), the estimation error was found to range from 9% to 21%.
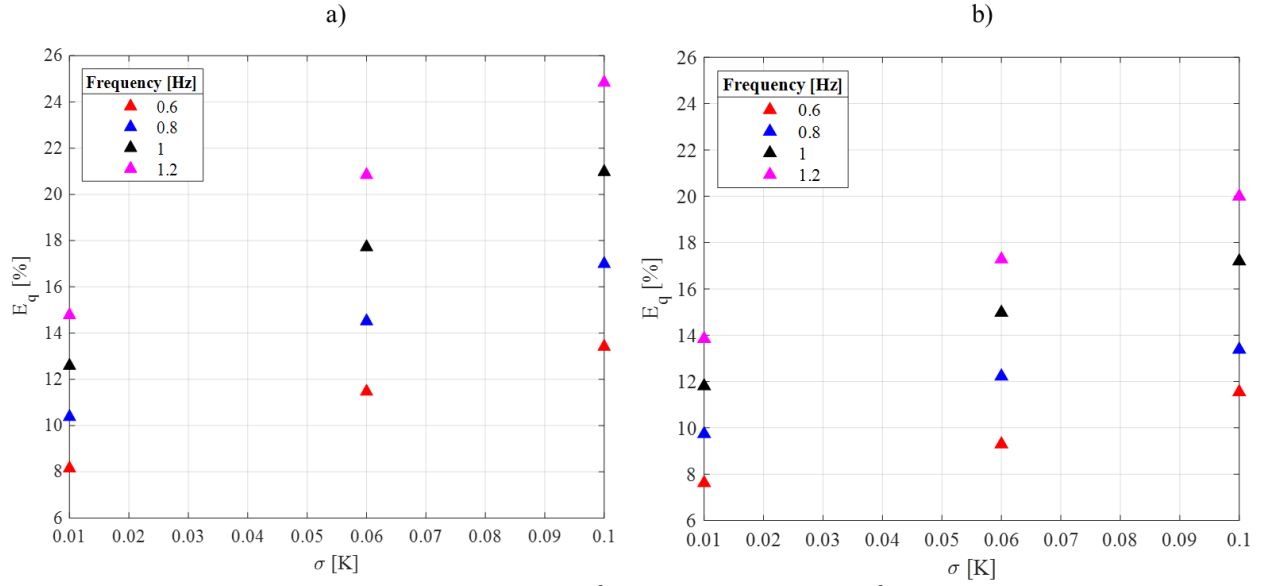
Figure 5: Estimation error for $A = 2000$ W/m^2 (a) and $A = 4000$ W/m^2 (b), considering oscillation frequencies between 0.6 and 1.2 Hz.

5. Results and discussion

The described estimation procedure was applied to the IR acquisitions obtained during the 67th Parabolic Flight Campaign (PFC) promoted by the European Space Agency (ESA). For each power input given to the evaporator, multiple tests were performed to evaluate the repeatability of the observed phenomena: Table 2 reports the power inputs given to the evaporator, together with the number of tests performed for each heat load.

Table 2: Number of tests, for each power input given to the evaporator.

Power input [W]	Number of tests
34	4
51	10
68	11
100	5
135	4
202	6

The inverse approach has been applied to each of the 10 PHP channels (Fig. 2), for each test case. In Fig. 6, for illustrative purposes, the measured temperature distribution along the axial coordinate over a 20 seconds time span is reported for power input equal to 100 W, channel 1.
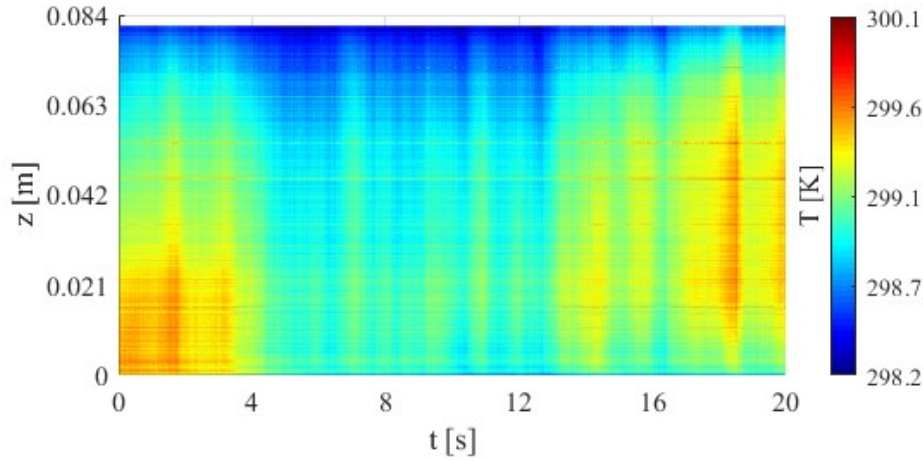
Figure 6: Measured wall temperature distribution for power input of 100 W, channel 1

The corresponding evaluated wall-to-fluid heat flux distribution, obtained by the IHCP solution approach, is reported in Fig. 7. As already described by the reference system of Fig. 4, the wall-to-fluid heat flux assumes positive values when the thermal energy is transferred from the fluid to the tube wall, i.e. the wall warms up.
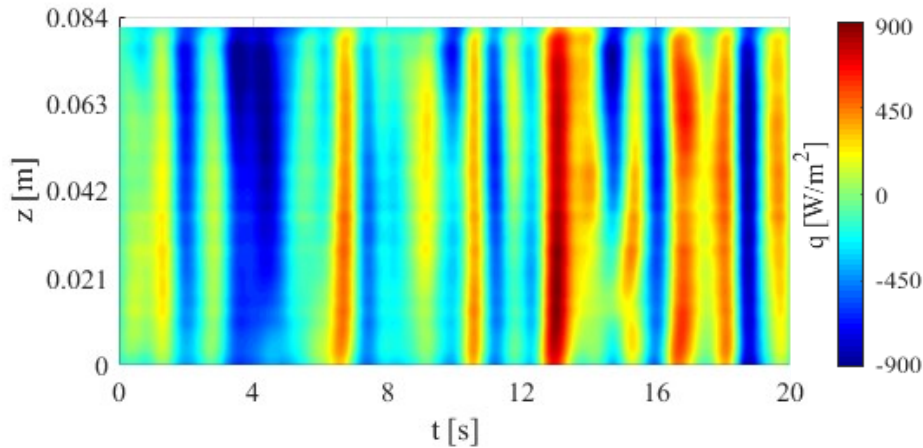

Figure 7: Estimated wall-to-fluid heat flux distribution, for power input of 100 W, channel 1.

As already stated in [9], the heat flux distribution over time provides useful information about the fluid dynamics of the device: positive heat fluxes correspond to the passage of hot vapor plugs and liquid slugs from the evaporator to the condenser. Negative heat fluxes denote instead flow reversals phenomena, during which cold fluid flows from the condenser to the evaporator at a lower temperature than that of the channel wall, previously heated by hot fluid coming from the evaporator. Such oscillatory behaviour is evident, in Fig. 7, from the alternance of positive and negative heat flux peaks.

5.1 Local heat flux distribution in transition

The device under study is classified as a hybrid Thermosyphon/Pulsating Heat Pipe: the transition between hyper and microgravity thus results in a transition between the Thermosyphon and the PHP working mode, where the flow pattern undergoes a sudden change due to the rising predominance of capillary forces with respect to buoyancy forces [25]. The experimental data reduction performed by Mangini et al. [11] on a similar PHP system revealed that the transition effects persist for some seconds after the onset of microgravity.
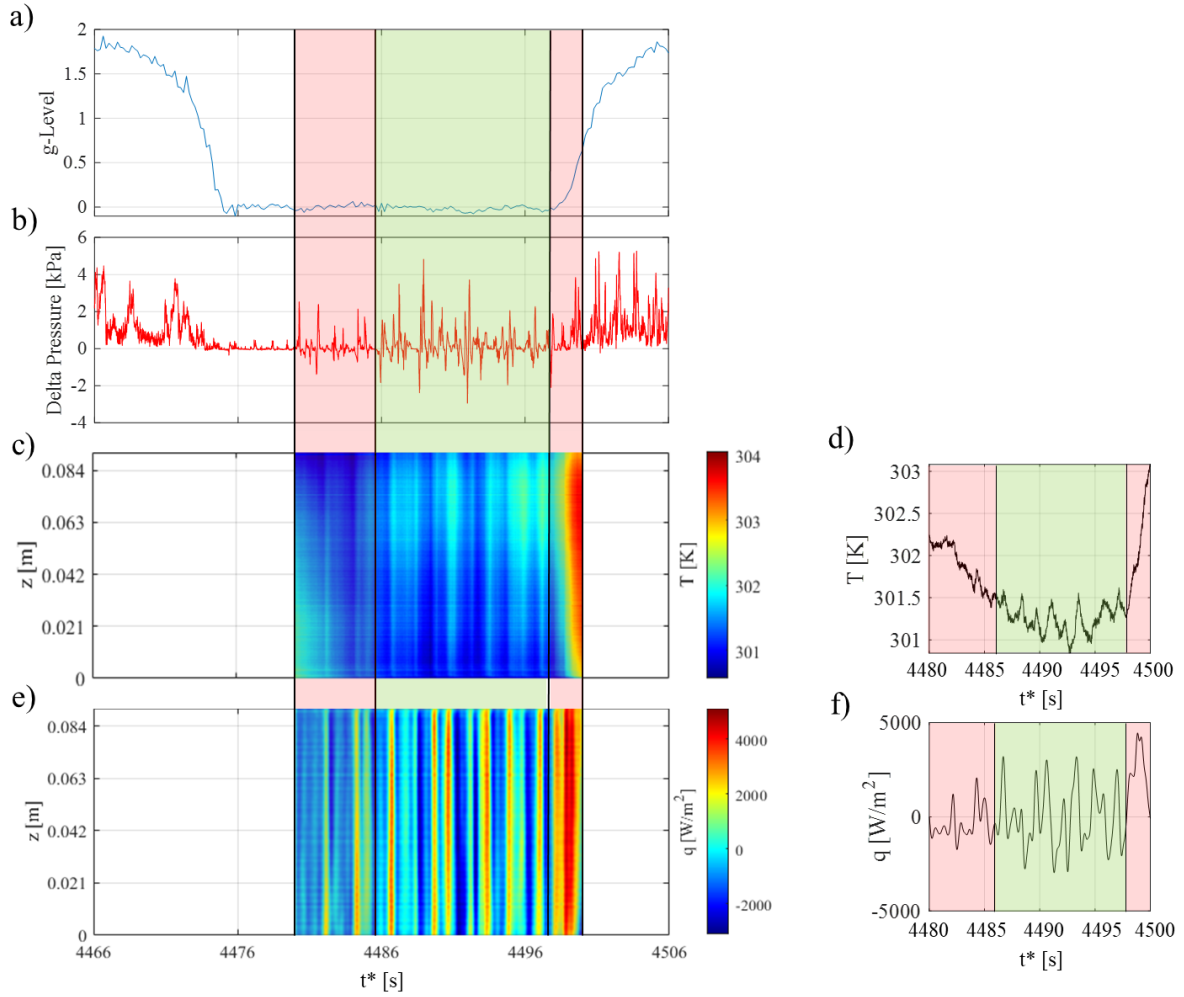
Figure 8: Gravity level (a), pressure difference (b), measured wall temperature (c), temperature distribution (axial coordinate = 0.045 m) (d), wall-to-fluid heat flux (e) and heat flux distribution (axial coordinate = 0.045 m) (f) over absolute time t*, referred to channel 1 and power input equal to 202 W.

In Fig. 8, they are reported the g-level (Fig. 8a), defined as the measured gravity field divided by 9.81 m/s², the fluid pressure difference Δp (Delta Pressure) between the evaporator and the condenser (Fig. 8b), the IR acquisition (Fig. 8c) and the corresponding wall-to-fluid heat flux (Fig. 8e) for power input to the evaporator equal to 202 W. The synchronization between the considered pieces of data was carried out by adopting the absolute time t*, where t* = 0 occurs at the pressure acquisition trigger during the flight.

In the reported example, both the wall temperature and the wall-to-fluid heat flux show appreciable oscillations, as clearly noticeable from the distributions of Figs. 8c-e. Two blow-ups of these distribution are a reported in Fig. 8d,f in order to easily catch this behaviour. According to [12], the consecutive variations of Δp from positive to negative values denote the presence of fluid motion between the evaporator and the condenser through those channels in which the fluid pressure measurement is performed. Consequently, the Delta Pressure of Fig. 8b exhibits clear fluid oscillations. Additionally, it must be underlined that, in the present study cases, the Delta Pressure and the IR acquisitions are not referred to the same channel but to two adjacent ones. However, for such high-power input to the evaporator, the fluid motion is simultaneously induced in every PHP channel [8], confirming that adjacent channels experience the same fluid oscillations. These results highlight that the estimated wall-to-fluid heat flux is thus capable of perceiving fluid oscillations likewise the pressure transducers, without the necessity to adopt any intrusive technique on the device layout.

Regarding the gravity field variation, the red-shaded areas of Fig. 8 are referred to time intervals in which the transition effects between hyper (g-level > 1) and micro-gravity (g-level = 0) are evident, while the green-

shaded areas are related to the time intervals in which the flow pattern is in a sort of stable condition, i.e. periodic oscillations with constant amplitude and frequency. In fact, after the hyper-gravity conditions, the wall temperature decreases almost monotonically, even though some fluid oscillations are still appreciable from Fig. 8f. These remarks confirm the presence of a settling period after the transition from hyper-gravity to micro-gravity. On the contrary, after such transition, the wall temperature (Fig.8d) fluctuates around a constant value, while the heat flux presents almost regular oscillations in terms of amplitude and oscillation frequency, thus denoting that the PHP is working in stable conditions.
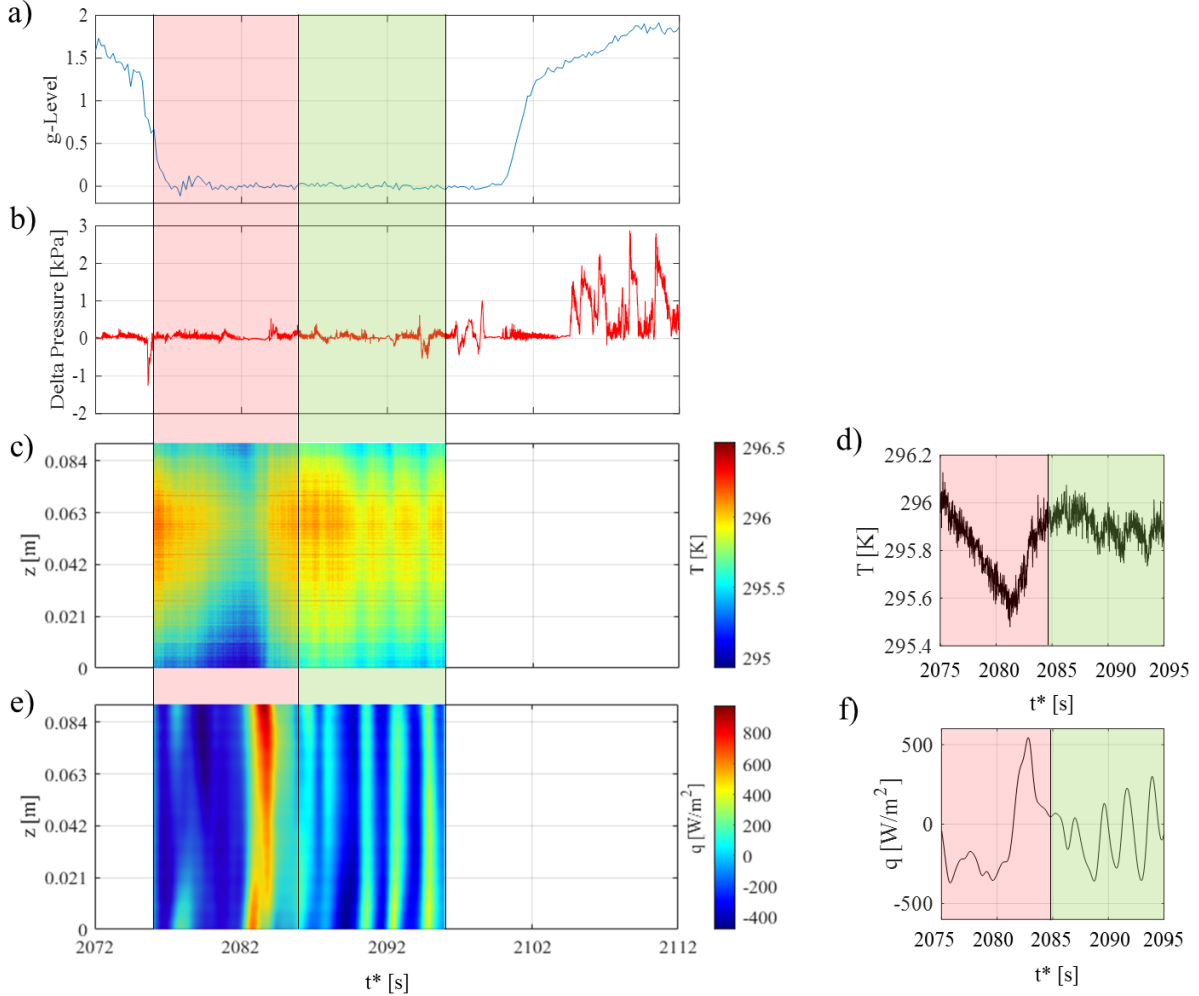

Figure 9: Gravity level (a), pressure difference (b), measured wall temperature (c), temperature distribution (axial coordinate = 0.045 m) (d), wall-to-fluid heat flux (e) and heat flux distribution (axial coordinate = 0.045 m) (f) over absolute time t*, referred to channel 1 and power input equal to 34 W.

In Fig. 9, the same analysis is reported for power input equal to 34 W. Similarly to the case of Fig. 8, the evaluated heat flux (Figs. 9e-f) is capable of describing the fluid oscillations, although, for low power inputs, the accordance between the wall-to-fluid heat flux and the Delta Pressure (Figs. 9b) is not always verified. It is probably due to the fact that pressure sensors and the IR acquisitions are not referred to the same channel and, for low power inputs, every channel works independently.

As observed in the previous example, the transitional phase (red-shaded area) is characterised by differences in terms of wall temperature and wall-to-fluid heat flux trends, with respect to those assessed within the stable PHP working mode (green-shaded area)..

5.2 Local heat flux distribution in stable working mode
Being the present investigation mainly focused on the study of the stable PHPs working mode in microgravity conditions, the transition period is ignored in the following analysis, thus considering just 10 of the 20 seconds of acquisition in microgravity

In order to highlight the fluid motion characteristics, Figs. 10-12 show the measured temperature distributions and the corresponding estimated heat flux distributions of four channels (i.e. 1, 5, 7 and 8), for three different power inputs to the evaporator: low power (34 W), intermediate power (100 W) and high power (202 W).
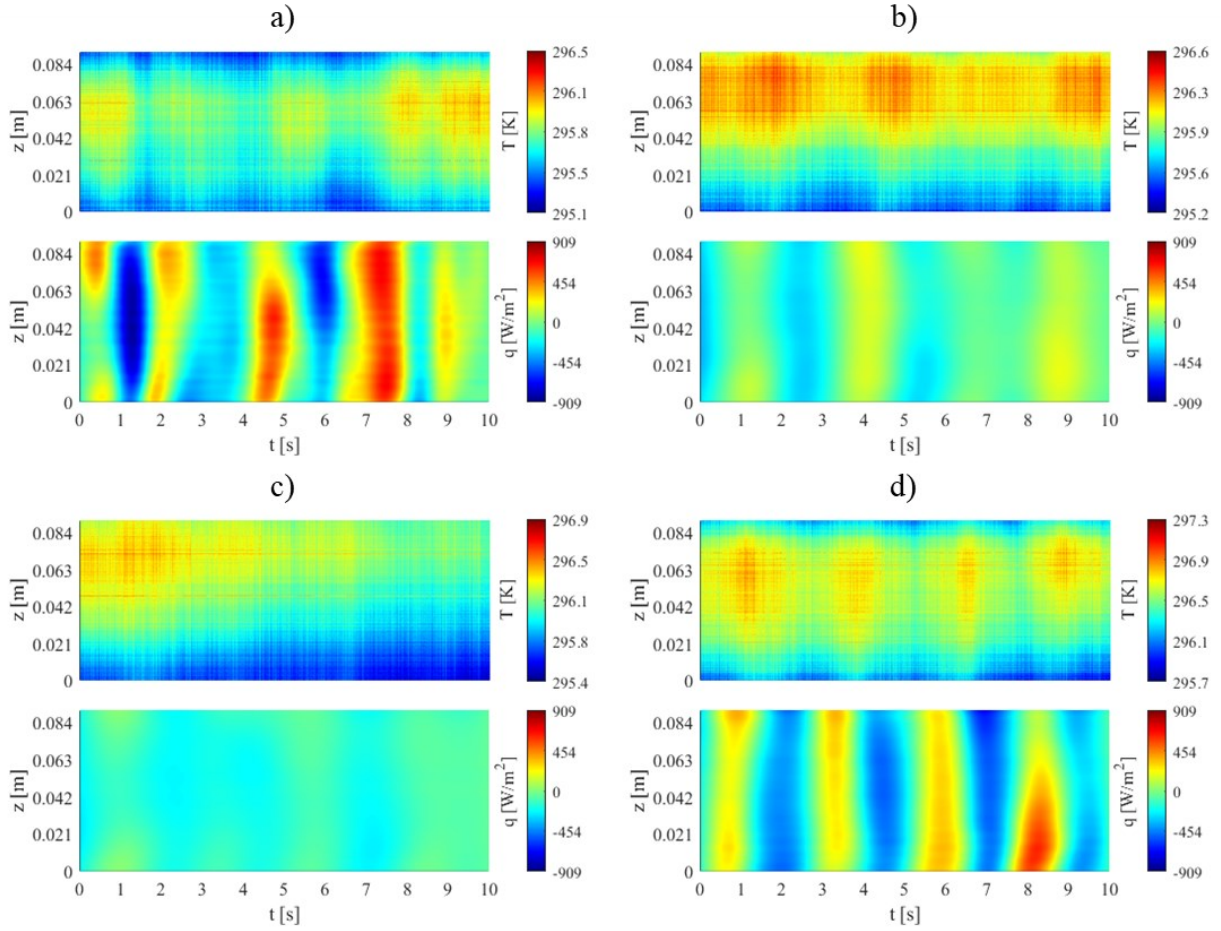

Figure 10: Wall temperature distributions and corresponding estimated heat fluxes for channel 1 (a), 5 (b), 7 (c) and 8 (d) for power input equal to 34 W.

For low power inputs, the device response differs from channel to channel; in fact, some channels present a slight fluid oscillation (Figs. 10a, 10d), described by the alternance of weak positive and negative peaks with low oscillation frequency, while other channels (Figs. 10b, 10c) are almost inactive, i.e. the heat flux is almost null within the whole distribution, except for some weak oscillations. This behaviour highlights that the power input is not able to thermally drive the fluid in the whole device, i.e. the PHP is not fully activated. The full activation of the device occurs when an appreciable fluid motion can be assessed in every PHP, with regular oscillations in terms of heat flux amplitude and oscillation frequency.

By increasing the power input up to 100 W, the oscillations become generally stronger, with higher heat flux amplitudes and oscillation frequencies (Fig. 11), although some small differences of behaviour among the channels are still present. The device is very close to the full activation.

For power input equal to 202 W (Fig.12), the fluid oscillation is thermally induced in every channel; the oscillations are stable, with high heat flux amplitudes and oscillation frequencies and no significant variations among the channels behaviour are observed. Hence, the device is completely activated, and the PHP oscillating behaviour involves all the channels, with similar characteristics.
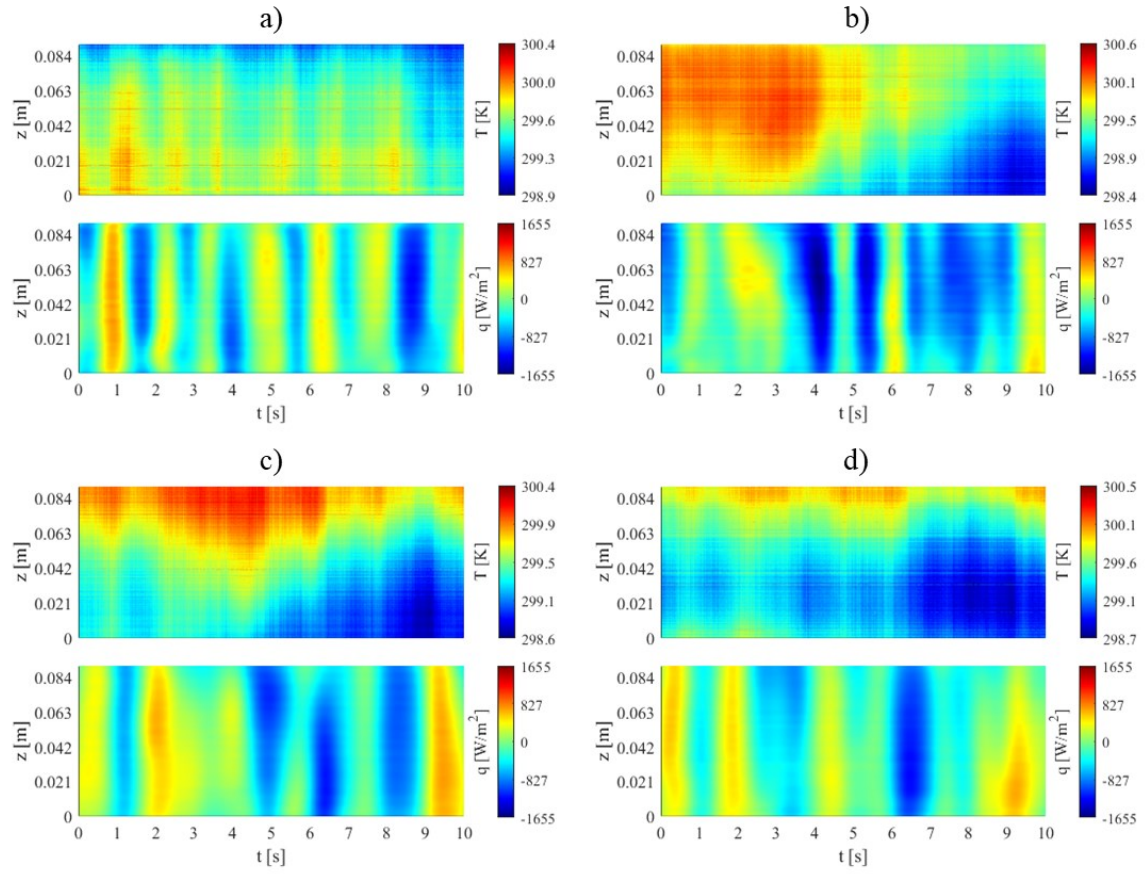
Figure 11: Wall temperature distributions and corresponding evaluated heat fluxes for channel 1 (a), 5 (b), 7 (c) and 8 (d), for power input equal to 100 W.
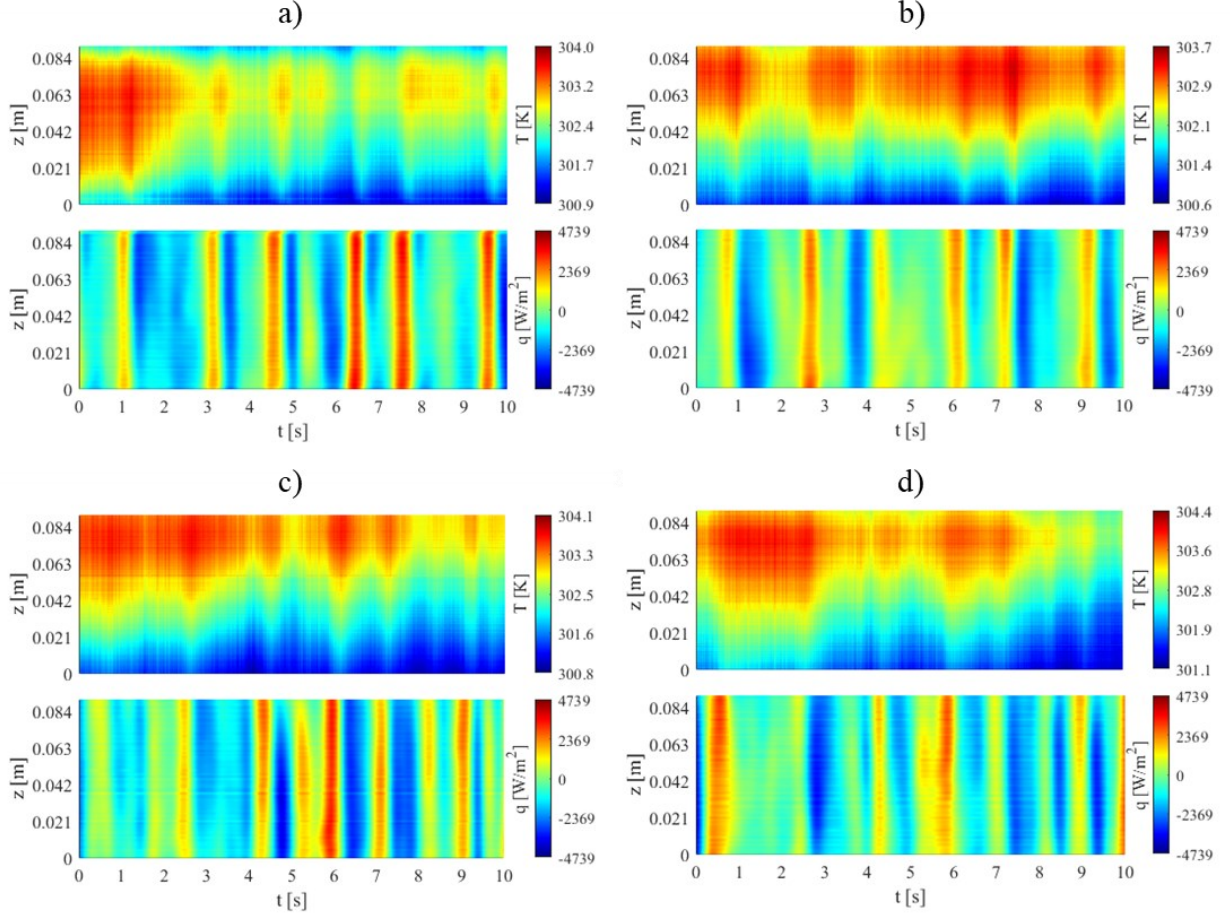
Figure 12: Wall temperature distributions and corresponding evaluated heat fluxes for channel 1 (a), 5 (b), 7 (c) and 8 (d), for power input equal to 202 W.

5.3 Coefficients of variation

The inverse heat transfer approach provides a massive amount of data about local time-space heat fluxes exchanged at the wall-fluid interface that needs to be adequately reduced in order to be efficaciously employed. In order to precisely quantify the thermal behaviour of the PHP in terms of time and space distribution of the wall-to-fluid heat flux in every channel, two coefficients, related to heat flux variations over time (cvt) and along space (cvs), respectively, are introduced [26]. Specifically, these statistical quantities define the regularity of a given sample in terms of oscillations. For example, for constant functions the coefficient of variation is equal to 0%; for sinusoidal functions it is around 50%, while functions having irregular amplitude present greater values.

The two coefficients, for the n-th channel, are defined as follows:

$$cvt_n = \frac{\sum_{i=1}^{N}\left[\dfrac{std(|q_n(i, t = 1, .., M)|)}{mean(|q_n(i, t = 1 ..., M)|)}\right]}{N} \tag{18}$$

$$cvs_n = \frac{\sum_{t=1}^{M}\left[\dfrac{std(|q_n(i = 1, ..., :N, t)|)}{mean(|q_n(i = 1, ..., :N, t)|)}\right]}{M} \tag{19}$$

where *std* and *mean* refer to the standard deviation and the arithmetic mean, respectively. M and N are the rows (axial coordinates) and the columns (time instants) of the generic heat flux distribution, respectively, while q_n is the heat flux amplitude of the n-th channel. The ratio of the standard deviation to the mean of q_n is averaged either for every i-th space coordinate (Eq. 18) or for every t-th time instant (Eq. 19) since the

employment of a single time-space coordinate, from a statistical point of view, is not representative of the actual variation of the time-space heat flux distributions.

Considering a generic channel, when the wall-to-fluid heat flux presents regular oscillations amplitude, *cvt* assumes low values; on the other hand, when the heat flux oscillation presents an irregular trend, *cvt* assumes high values.

Analogously, *cvs* is high when great variations of the heat flux are appreciable along the channel, while it assumes low values when the whole channel is simultaneously interested by the same thermal phenomenon.

Figure 13 shows the statistical analysis applied to the present investigation for every power input: *cvt* (red shade) and *cvs* (blue shade) were evaluated for every analysed channel.
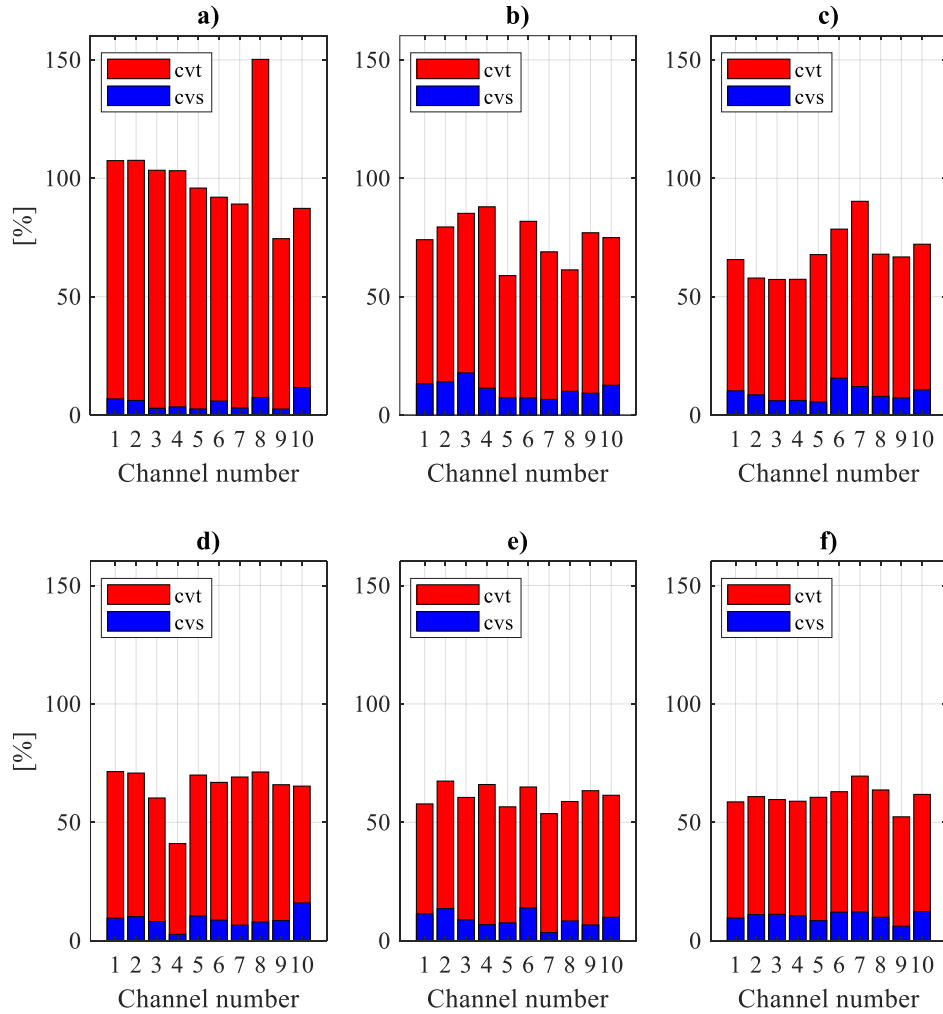

Figure 13: Coefficients of variation *cvt* and *cvs*, referred to time (red) and space (blue) variations of the evaluated wall-to-fluid heat flux in each channel, respectively, for power input equal to 34(a), 51(b), 68(c), 100(d), 135 (e) and 202 W (f).

For the lowest power input (Fig. 13a), the *cvt* assumes high values and differs significantly from channel to channel, confirming that the fluid motion has a great variability over the entire device and the heat flux oscillations are not stable, thus highlighting that the PHP is not fully activated. The coefficient of variation in time decreases as the power input increases, also presenting a lower variability from channel to channel (Fig 13 b). For higher power inputs (Fig. 13c-d), the coefficient of variation is about 50% and almost constant among every channel, confirming that the PHP is fully activated and characterised by regular fluid oscillations. In the same figure, the blue charts are instead referred to the coefficient of variation in space, obtained by means of Eq. (13): for every considered power input given to the evaporator, *cvs* is characterised by low values, with no great variations from channel to channel even for the lowest examined power input (Fig. 13a).

5.4 Frequency analysis

The study of the fluid oscillation frequency is crucial for understanding the PHP working principles since the thermally induced oscillations are responsible for efficient heat dissipation [27]. The core issue regarding the fluid oscillation frequency evaluation can be referred to the non-fixed oscillation frequency of the fluid between the evaporator and the condenser section due to the chaoticity of the thermofluidic system [28]. Hence, the fluid oscillation frequency in PHPs is usually defined by a peak in the power spectrum, i.e. dominant frequency, of a given measured set of data [29]. Among other commonly employed estimation methods, such as the fast Fourier transform, the short-time Fourier transform and the Hilbert-Huang transform [7,30], Perna et al. [17] suggested the use of the wavelet transform approach for the dominant frequency evaluation. Specifically, the Morlet wavelet [31] analysis performed on the fluid pressure signal, has been proven to be more suitable than the tube wall temperature, for the fluid dominant oscillation frequency evaluation in PHPs.

The outputs of the wavelet analysis are the magnitude scalogram, which represents the power related to each frequency over the sample duration, and the power spectrum, which is the time integral of the magnitude scalogram, for every frequency. Specifically, the scalogram enables to identify the main oscillation frequencies of the analysed oscillatory phenomenon, i.e. the frequencies with the greatest related power over time, while the power spectrum defines the frequency with the greatest power within the entire observation window. According to Perna et al. [17], the dominant frequency is here defined as the maximum value of the wavelet power spectrum.

As previously highlighted, the wall-to-fluid heat flux is strictly linked to the working fluid oscillation. Hence, single axial coordinates of the local heat flux distributions are processed by means of the 1-D wavelet transform approach to evaluate the fluid dominant oscillation frequency. The wavelet parameters adopted in the present study are listed in Table 3.

Table 3: wavelet parameters.

a [1/Hz]	71
ω_0	2π
f_{min} [Hz]	0.1
f_{max} [Hz]	18

It must be highlighted that the analysis was limited to fluid oscillation frequencies higher than 0.5 Hz, due to the fact that the analysed time window is limited to 10 seconds, thus preventing the possibility to observe a sufficient number of peaks corresponding to dominant frequencies lower than 0.5 Hz. For the present application, the uncertainty of the dominant frequency was found to be equal to 0.06 Hz.

In order to test the robustness of this approach, the wavelet analysis was replicated for different axial coordinates of the same heat flux distribution referred to one channel: the resulting f_D doesn't change along the channel, thus confirming the non-dependency of the oscillation frequency on the axial coordinate.

The wavelet transform analysis was then performed for all the study cases. In Figs 14-16, the wavelet transform approach was applied to the wall-to-fluid heat fluxes referred to three different power inputs to the evaporator, for three representative channels, i.e. channel 1, 5 and 8 (z = 0.045 m). For low power input (Fig. 17), the dominant oscillation frequencies were found to be generally low (around 0.6 Hz). The presence of channels in which a dominant frequency couldn't be appreciated confirms what already observed in the previous section, where the wall-to-fluid heat flux distributions showed a partial activation of the device.

The dominant fluid oscillation frequency increases with the power input (Figs. 15-16), and the fluid oscillations become more and more repeatable within the overall device, thus denoting a full activation of the PHP. However, power spectrum of Fig. 16c presents different powers related to each dominant frequency, hence the repeatability of the oscillatory phenomenon cannot be fully stated. This is mainly due to the limited observation window, which does not allow a complete characterization of the PHP chaotic behaviour.

Figure 14: Magnitude scalograms (a), wall-to-fluid heat fluxes (single axial coordinate) (b) and power spectrum (c), for power input equal to 34 W, channels 1, 5 and 8.
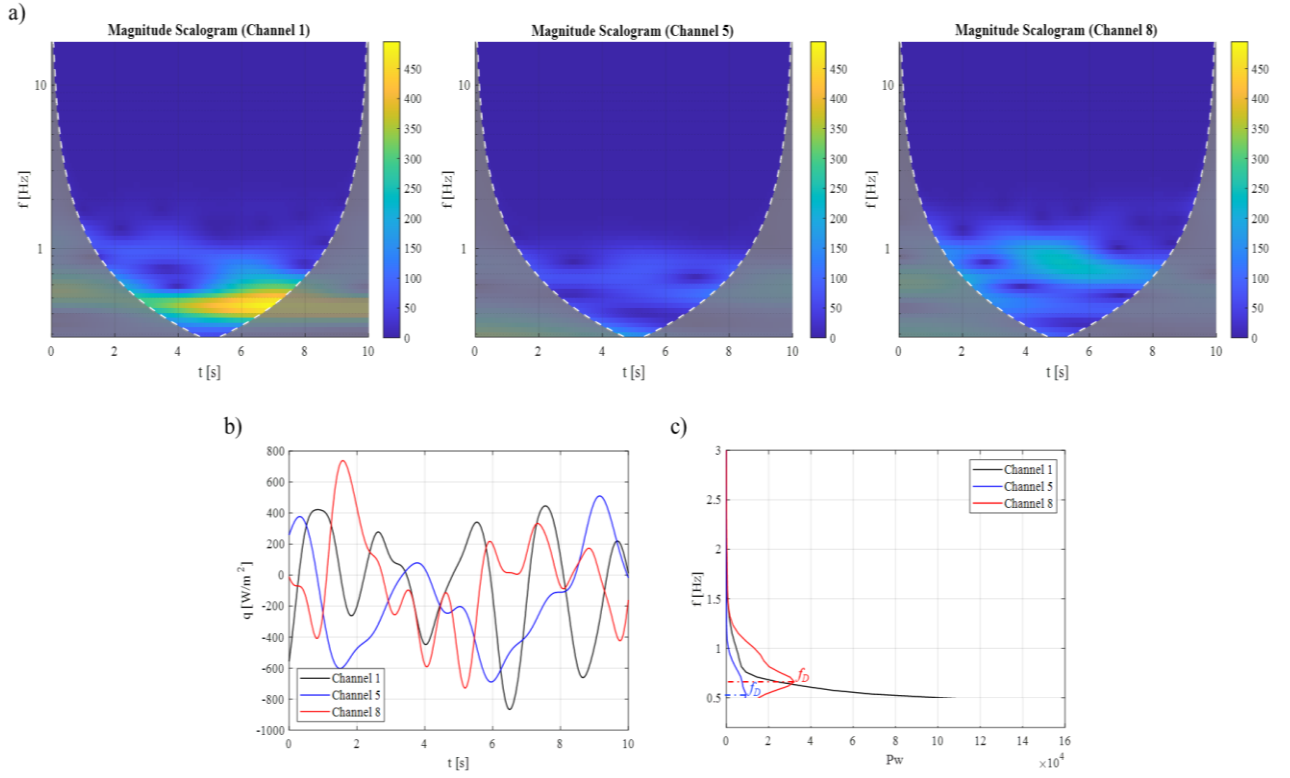

Figure 15: Magnitude scalograms (a), wall-to-fluid heat fluxes (single axial coordinate) (b) and power spectrum (c), for power input equal to 100 W, channels 1, 5 and 8.
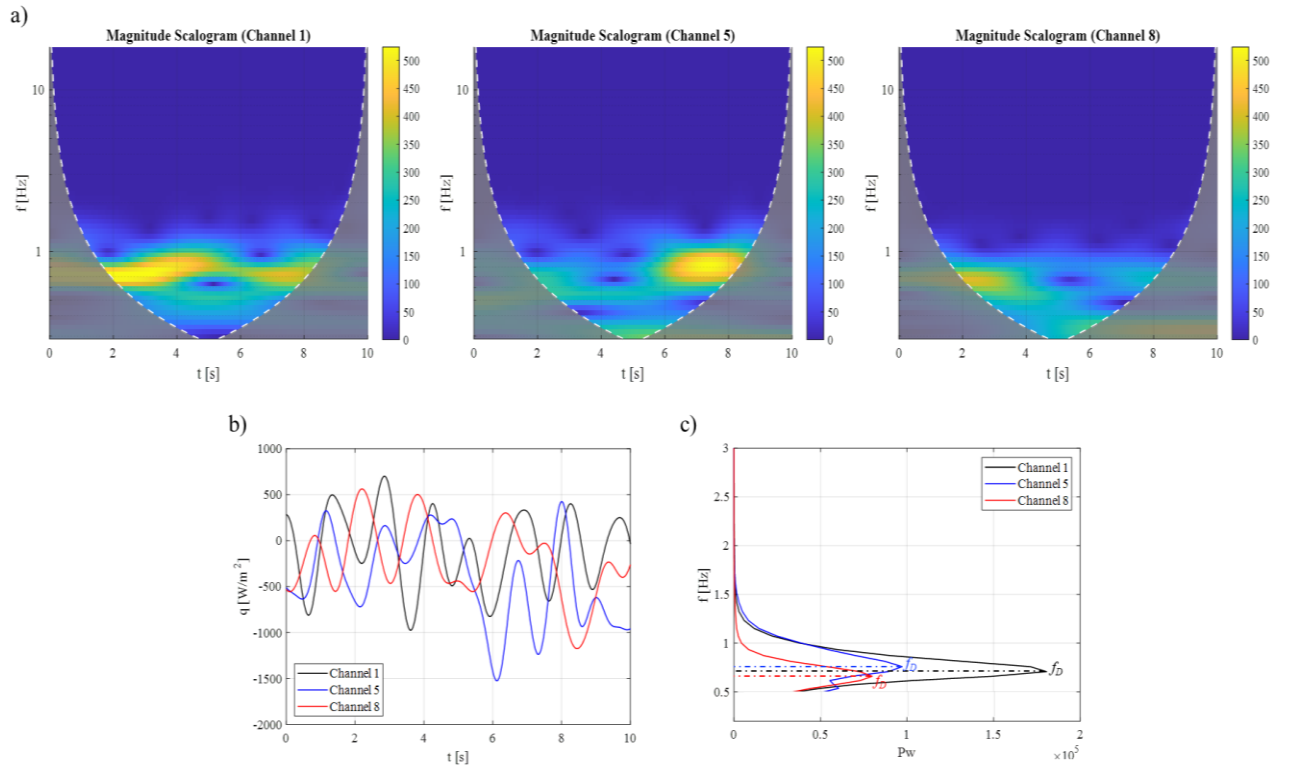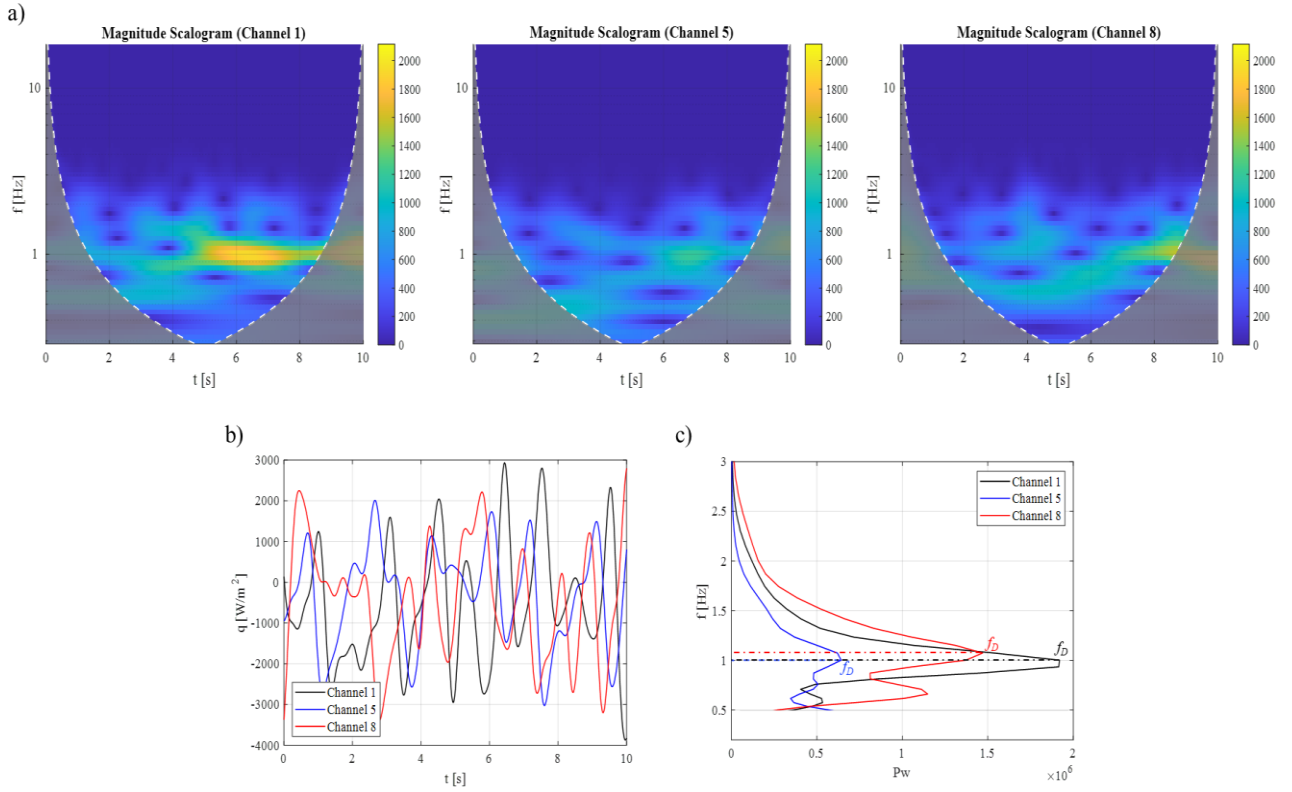
Figure 16: Magnitude scalograms (a), wall-to-fluid heat fluxes (single axial coordinate) (b) and power spectrum (c), for power input equal to 202 W, channels 1, 5 and 8.

Table 4 provides a sample of the evaluated dominant frequencies related to every channel, considering one test case of Table 2 for each power input to the evaporator. Here, the channel-wise oscillatory behaviour can be appreciated, highlighting that some PHP channels are inactive at low power inputs since a dominant frequency could not be evaluated (dashes), while the PHP is fully activated for high power inputs. Again, the dominant frequency has an increasing trend with the power input, although few channels still show a different oscillatory behaviour, i.e. different dominant frequencies, even at elevated power inputs.

Table 4: Dominant frequency for each PHP channel, referred to one test case for each power input.

f_D [Hz]		Power Input [W]					
		34	*51*	*68*	*100*	*135*	*202*
Channel number	*1*	-	-	-	0.71	0.81	0.93
	2	-	0.66	-	0.71	0.81	0.93
	3	0.58	-	0.62	0.71	0.81	0.93
	4	-	0.57	0.53	0.53	0.81	0.66
	5	-	0.57	0.61	0.76	0.58	1
	6	-	0.61	0.61	0.58	0.81	1
	7	0.54	0.61	0.57	0.58	0.81	1
	8	0.66	-	0.6	0.66	0.81	1.1
	9	-	0.5	0.57	0.71	0.76	0.9
	10	0.54	-	0.6	0.71	0.71	0.61

The frequencies reported in Table 4 confirm the variations in terms of local heat flux from channel to channel previously stated in Section 5.3 by means of *cvt*, thus underlining the accordance between the channel-wise statistical analysis of the heat flux amplitude and the channel-wise frequency analysis.

5.5 Amplitude analysis

In order to fully achieve a channel-wise description of the heat transfer phenomena, the average heat flux amplitude A_{av}, here defined as the average of the absolute wall-to-fluid heat flux distributions related to each analysed channel, is introduced.

In Table 5, A_{av} is reported for the same test cases of Table 4: considering each PHP channel, the average amplitude does not present any perceivable correlation with the dominant frequency, thus highlighting that the fluid oscillation frequency is not strictly linked to the heat transfer entity through the adiabatic section, although the both quantities seem to increase with the power input in every channel.

Table 5: Average wall-to-fluid heat flux amplitude for each PHP channel, referred to one test case selected among every analysed case for each power input.

A_{av} [W/m²]		Power Input [W]					
		34	51	68	100	135	202
Channel number	1	310	282	395	367	689	1295
	2	303	394	236	433	579	1383
	3	355	325	325	490	658	1440
	4	255	262	283	507	564	1092
	5	274	331	341	491	578	933
	6	192	216	379	503	583	1228
	7	232	313	471	402	474	1261
	8	264	282	495	348	462	1269
	9	239	238	405	475	474	1215
	10	171	312	408	340	484	1102

5.6 Statistical approach

It has to be pointed out that A_{av} (Table 5) and f_D (Table 4) were evaluated by considering one test case for each power input to the evaporator in order to focus on the variation of such quantities from channel to channel. However, the plenty of results provided by the discussed post-processing procedure suggests the employing of a statistical investigation on every test case to quantify the wall-to-fluid heat flux amplitude and the dominant oscillation frequency for each power input, thus achieving a global characterization of the PHP thermal behaviour. To this aim, the totality of the time-space heat flux distributions (absolute value), evaluated for every test case of Table 2, was first used as input parameter for the cumulative distribution function Φ [12], defined as the probability that the wall-to-fluid heat flux amplitude q will assume a value less than or equal to a generic heat flux amplitude q_0. Calling $a_0 \in [0,1]$ a value assumed by $\Phi(q)$, the inverse cumulative distribution function $q_0 = \Phi^{-1}(a_0)$ represents the $[a_0 \cdot 100]^{th}$ percentile of the analysed distribution. Consequently, any percentile of the heat flux distribution can be easily identified by means of such distribution function.

$\Phi(q)$ is reported in graph of Fig. 17, for every power input to the evaporator: for power inputs ranging from 34 to 100 W, the cumulative distribution function presents comparable trends, denoting similar statistical distributions for q, even though the curve related to 34 W undergoes a sharp change in shape for $\Phi(q) > 0.9$ due to the strong and sporadic heat flux peaks occurring during the PHP intermittent working mode. By increasing the heat load, $\Phi(q)$ progressively flattens, confirming the variation in the working behaviour (PHP full activation) that results in higher wall-to-fluid heat flux amplitude within the whole statistical distribution.
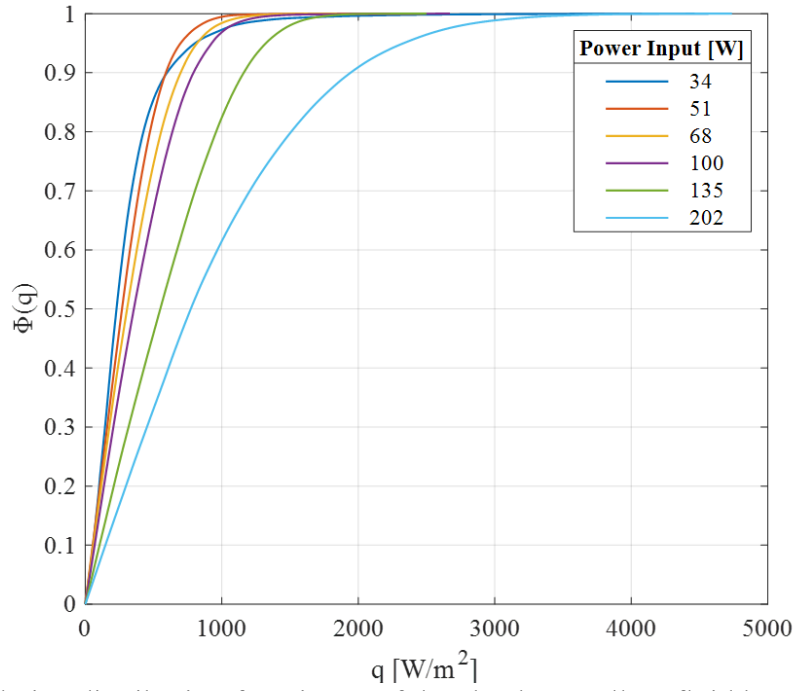
Figure 17: Cumulative distribution function Φ of the absolute wall-to-fluid heat flux q, for every power input given to the evaporator.

The 80th percentile is typically adopted among other statistical quantities due to its capability of removing from the analysis the outliers having no statistical meaning, i.e. those peaks of wall-to-fluid heat flux that occur sporadically. For this reason, in order to quantitatively define the PHP working regimes, the 80th percentile of the heat flux amplitude, q_{80}, corresponding to $\Phi(q) = 0.8$, is reported in Fig. 18 as a function of the power input. Here, the q_{80} is almost constant at low power inputs, verifying the similar wall-to-fluid thermal interactions during the intermittent functioning mode. From 100 W up to the maximum power input, the heat flux amplitude increases almost linearly with the power input, confirming the increasing entity of the wall-to-fluid thermal interactions within the adiabatic section during the full activation functioning mode.
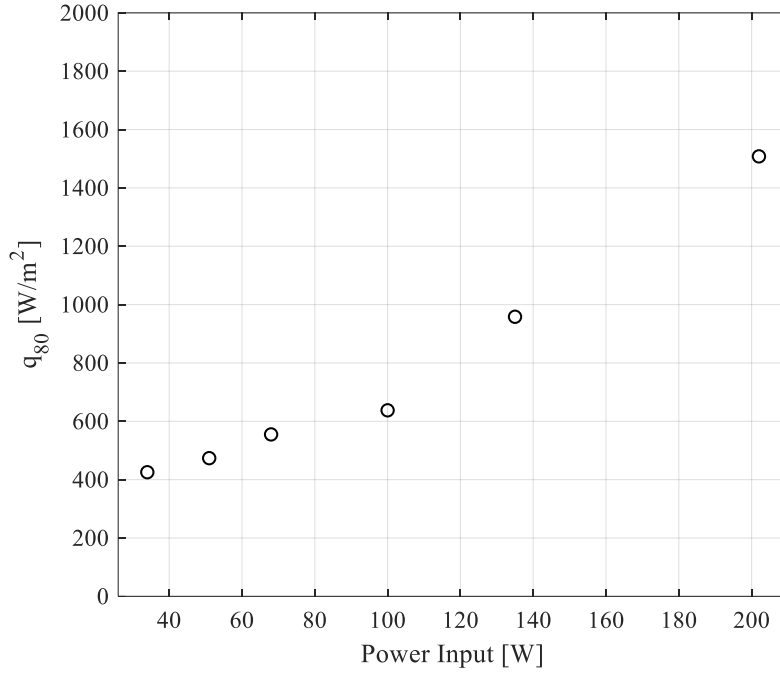
Figure 18: 80th percentile of the wall-to-fluid heat flux amplitude,
evaluated by considering every test case of Table 2.

The dominant frequencies, related to every test case of Table 2 and every analysed PHP channel, are similarly processed by computing the 80th percentile of the fluid oscillation frequency $f_{D,80}$ and reported in Fig. 19. The same figure enables to compare between the presented $f_{D,80}$t o the f_D observed by Perna et al. [17] for the same test conditions. In [17] the dominant frequency was evaluated by processing the fluid pressure acquisitions referred to a single channel. The agreement between both pieces of data is thus assessed, thus confirming the effectiveness of the adopted IR non-intrusive technique. Moreover, during the intermittent flow regime, $f_{D,80}$ does not change substantially, while it increases during the device full activation and seems to settle around constant values for high power inputs to the evaporator (> 135 W).
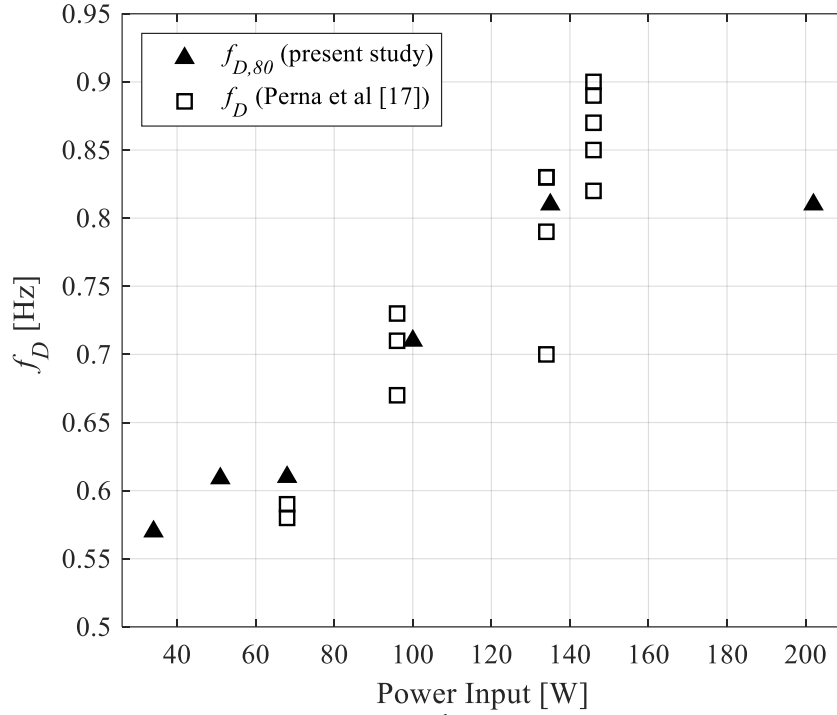
Figure 19: Comparison between the 80th percentile of the dominant frequency and the dominant frequencies obtained by Perna et al. [17], for the same study cases, by processing the fluid pressure signals referred to one single PHP channel.

As a final point, a new coefficient of variation, *cvf*, is introduced to quantify frequency variations for every power input *P*:

$$cvf(P) = \frac{std(f_{D,80}(P))}{mean(f_{D,80}(P))} \tag{20}$$

In Fig. 20, *cvf* is shown as a function of the power input to the evaporator. The channels in which no fluid oscillation could be perceived were assumed to have $f_{D,80} = 0$ Hz. Such statistical coefficient quantifies the deviation of f_D from its mean value: when *cvf* is high, the analysed population presents some values which strongly differ from the others. On the contrary, when *cvf* is low, the given population presents similar values. In fact, when *cvf* is equal to 0 %, the population is entirely constituted by equal values.

For low power inputs, *cvf* is high, denoting that fluid oscillation occurs in few channels. *cvf* gradually decreases with the power input during the intermittent flow regime since some channels start to exhibit fluid oscillations. From 135 W to the maximum power input, *cvf* is low and almost constant, denoting that the device is working in optimal conditions (full activation) and the dominant oscillation frequencies are similar for each heat load, although a slight variation from channel to channel is still appreciable within every test case, *i.e. cvf is always more than 20.*
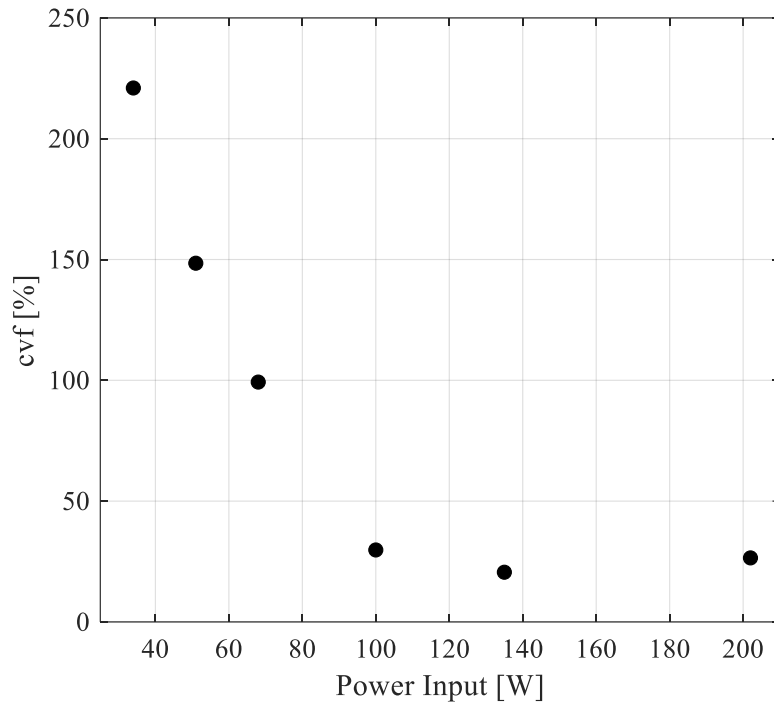
Figure 20: *cvf* against power input, obtained by considering the dominant oscillation frequencies related to every PHP channel and all the test cases of Table 2; when the channels did not exhibit any fluid oscillation, the dominant frequency was assumed equal to 0 Hz.

In conclusion, the present statistical investigation enabled to clearly identify the transition between the intermittent flow working regime (sporadic fluid motion, occurring in some channels) and the full activation working regimes (continuous fluid motion within the whole adiabatic section) by the statistical quantities introduced in the present work (i.e., q_{80}, $f_{D,80}$ and *cvf*). In particular, for all these quantities, the trend slope changes in the range 60 ÷ 90 W, confirming that, at low power inputs, the device is not yet fully activated, while at high power inputs the fluid oscillation is promoted in every channel.

5. Conclusions

A multi-turn PHP, tested during the 67th PFC promoted by the ESA, was thermally characterised by evaluating the local wall-to-fluid heat fluxes in microgravity conditions with high spatial resolution. Specifically, the Inverse Heat Conduction Problem (IHCP) was solved in the wall, starting from the IR measurements carried out on the external wall of the PHP adiabatic section. The heat flux amplitudes related to each PHP channel were studied by means of the coefficients of variation. A frequency analysis was additionally carried out on the heat flux. An original statistical analysis was finally performed, thus focusing on the correlation between the heat flux amplitude, the fluid oscillation frequency and the power input given to the evaporator. The main research outcomes are:

- The fluid motion through each PHP channel can be successfully assessed by the wall-to-fluid heat flux which, conveniently elaborated, enables to identify the transition from intermittent flow (sporadic fluid motion, occurring in some channels) to full activation (stable fluid motion within the whole adiabatic section,).
- The coefficient of variation over time *cvt* allows the identification of the PHP working regimes: during the intermittent flow regime, *cvt* is high and varies significantly from channel to channel, while the full activation of the device is outlined by low and almost constant values of *cvt* within the whole adiabatic section.
- The fluid oscillation frequency investigation confirms the existence of two working regimes, depending on the power input given to the evaporator. During the intermittent flow regime, many channels do not

present any fluid oscillation frequency; on the contrary, for high power inputs to the evaporator, the dominant frequency f_D is generally similar in the whole adiabatic section, even though the oscillatory behaviour may still vary from channel to channel.

- The statistical analysis of the heat flux amplitude and frequency, carried out by considering every PHP channel within all the test cases, permits to easily identify the transition between the two PHP working regimes. For the studied device, such transition occurs in the range $60 \div 90$ W.
- The results of the presented statistical approach are in good agreement with the dominant frequency estimated with pressure sensors by Perna et al. [17] within a single PHP channel in the same test conditions.

In conclusion, the non-intrusive approach presented in this work is capable of providing similar information regarding the fluid motion inside the PHP to those obtained by the traditional intrusive experimental methods (e.g. direct fluid temperature-pressure measurements) or transparent inserts (e.g. sapphire tube), which perturb the original layout of the PHP and require a complex experimental set-up. Moreover, the provided local heat transfer properties, also identified in terms of statistical distributions, can be used for the design and benchmarking of accurate numerical models of multi-turn PHPs.

Nomenclature

Symbol	Quantity	SI Unit
a	Scale dilation parameter	1/Hz
A_{av}	Average heat flux amplitude	W/m^2
c_p	Specific heat at constant pressure	J/kg·K
cvf	Coefficient of variation (dominant frequency)	%
cvs	Coefficient of variation (space)	%
cvt	Coefficient of variation (time)	%
E_q	Estimation error	%
f_D	Dominant frequency	Hz
h	Convective heat-transfer coefficient	W/m^2·K
H	Transfer function	-
k	Thermal conductivity	W/m·K
P	Power input to the evaporator	W
q	Convective heat flux	W/m^2
Q	Power	W
r	Radial coordinate	m
R_{env}	Overall heat-transfer resistance between the external tube wall and the surrounding environment	m^2·K/W
s	Wall thickness	m
t	Time	s
T	Temperature	K
t^*	Absolute time	s
u, v	Frequency components	rad^{-1}
u_c	Cut-off frequency	rad^{-1}
z	Axial coordinate	m

α	Angular coordinate	rad
ρ	Density	kg/m^3
σ	Noise level	K
τ	Time constant	s
Φ	Cumulative distribution function	-

Subscripts, superscripts

80	80th percentile
env	environment
ext	external
f	filtered
in	inner
int	internal

References

[1] D. Bastakoti, H. Zhanga, D. Lia, W. Caia, F. Li, An overview on the developing trend of pulsating heat pipe and its performance, App. Therm. Eng. 141 (2018) 305–332.

[2] V. Nikolayev, M. Marengo, Pulsating heat pipes: basics of functioning and numerical modeling, ISBN 978-981-3234-36-9, in: J.R. Thome (Ed.), Encyclopedia of Two-Phase Heat Transfer and Flow IV, vol. 1 Modeling of Two-Phase Flows and Heat Transfer, World Scientific, 2018.

[3] Xiaohong Han, Xuehui Wang, Haoce Zheng, Xiangguo Xu, Guangming Chen, Review of the development of pulsating heat pipe for heat dissipation, Renewable and Sustainable Energy Reviews, 59 (2016), 692-709.

[4] T. H. Kim, E. Kommer, S. Dessiatoun, J. Kim, Measurement of two-phase flow and heat transfer parameters using infrared thermometry, International Journal of Multiphase Flow, 40 (2012), 56-67.

[5] Trainer D., Kim J., & Jin S., Heat transfer and flow characteristics of air-assisted impinging water jets. International Journal of Heat and Mass Transfer, 64 (2013), 501–513.

[6] S.D. Farahani and M. Karami, Experimental estimation of local heat flux on boiling surface in a mini-channel, International Communications in Heat and Mass Transfer, 108 (2019), 104271.

[7] M. Mameli, M. Marengo, S. Khandekar, Local heat transfer measurement and thermo-fluid characterization of a pulsating heat pipe, International Journal of Thermal Sciences, 75 (2014), 140-152.

[8] J. Jo, J. Kim, S. Jin Kim, Experimental investigations of heat transfer mechanisms of a pulsating heat pipe, Energy Conversion and Management, 181 (2019), 331-341.

[9] Cattani, L., Mangini, D., Bozzoli, F., Pietrasanta, L., Mameli, M., Filippeschi, S., ... & Marengo, M. (2019). An original look into pulsating heat pipes: Inverse heat conduction approach for assessing the thermal behaviour. Thermal Science and Engineering Progress, 10, 317-326.

[10] D. Mangini, M. Marengo, L. Araneo, M. Mameli, D. Fioriti, S. Filippeschi, Infrared analysis of the two-phase flow in a single closed loop pulsating heat pipe, Experimental Thermal and Fluid Science, 97 (2018), 304-312.

[11] D. Mangini, M. Mameli, D. Fioriti, S. Filippeschi, L. Araneo, M. Marengo, Hybrid Pulsating Heat Pipe for space applications with non-uniform heating patterns: Ground and microgravity experiments, Applied Thermal Engineering, 126 (2017), 1029-1043.

[12] M. Mameli, A. Catarsi, D. Mangini, L. Pietrasanta, N. Michè, M. Marengo, P. Di Marco, S. Filippeschi, Start-up in microgravity and local thermodynamic states of a hybrid loop thermosyphon/pulsating heat pipe, Applied Thermal Engineering, 158 (2019), 113771.

[13] Bishnu N. Mahapatra, P.K. Das, Sudhansu S. Sahoo, Scaling analysis and experimental investigation of pulsating loop heat pipes, Applied Thermal Engineering, 108 (2016), 358-367.

[14] J. Kim, S. J. Kim, Experimental investigation on working fluid selection in a micro pulsating heat pipe, Energy Conversion and Management, 205 (2020), 112462.

[15] D.-T. Vo, H.-T. Kim, J. Ko, K.-H. Bang, An experiment and three-dimensional numerical simulation of pulsating heat pipes, International Journal of Heat and Mass Transfer, 150 (2020).

[16] V.K. Karthikeyan, S. Khandekar, B.C. Pillai, P. K. Sharma, Infrared thermography of a pulsating heat pipe: Flow regimes and multiple steady states, Applied Thermal Engineering, 62 (2014), 470-480.

[17] R. Perna, M. Abela, M. Mameli, A. Mariotti, L. Pietrasanta, M. Marengo, S. Filippeschi, "Flow characterization of a pulsating heat pipe through the wavelet analysis of pressure signals", Applied Thermal Engineering, vol. 171, pp. 115-128, 2020.

[18] Catarsi A. Fioriti D., Mameli M., Filippeschi, S., Di Marco P., Accuracy analysis of direct infrared temperature measurements of two-phase confined flows, International Heat Transfer Conference, Volume 2018-August, 2018, Pages 8939-8953.

[19] Incoprera F.P., De Witt D.P., Fundamentals of Heat and Mass Transfer, John Wiley & Sons, Inc New York (2002).

[20] Beck J.V., Balckwell B., St. Clair Jr C.R., Inverse Heat Conduction – Ill-posed problems, New York: John Wiley & Sons Inc. 1985.

[21] Murio A.D., The Mollification Method and the Numerical Solution of Ill-Posed Problems, New York: John Wiley and Sons 1993.

[22] Delpueyo D., Balandraud X., Grédiac M., Heat source reconstruction from noisy temperature fields using an optimised derivative Gaussian filter, Infrared Physics & Technology *60* (2013) 312–322.

[23] Bozzoli F., Pagliarini G., Rainieri S., Experimental validation of the filtering technique approach applied to the restoration of the heat source field, Experimental Thermal and Fluid Science 44 (2013) 858-867.

[24] Morozov V.A., Methods for Solving Incorrectly Posed Problems, Springer-Verlag, New York, (1984).

[25] D. Mangini, M. Mameli, A. Georgoulas, L. Araneo, S. Filippeschi, M. Marengo, "A pulsating heat pipe for space applications: Ground and microgravity experiments", International Journal of Thermal Sciences, vol. 95, pp. 53-63, 2015

[26] B. Everitt, The Cambridge Dictionary of Statistics. Cambridge, UK New York: Cambridge University Press, 1998.

[27] G. Spinato, N. Borhani, J. R. Thome, Understanding the self-sustained oscillating two-phase flow motion in a closed loop pulsating heat pipe, Energy, 90 (2015), 889-899.

[28] K. Ishii, K. Fumoto, "Temperature visualization and investigation inside evaporator of pulsating heat pipe using temperature-sensitive paint", Applied Thermal Engineering, vol. 155, pp. 575-583, 2019.

[29] Xu, J.L., Zhang, X.M. Start-up and steady thermal oscillation of a pulsating heat pipe. Heat Mass Transfer 41, 685–694, 2005.

[30] J. D. Fairley, S. M. Thompson, D. Anderson, "Time–frequency analysis of flat-plate oscillating heat pipes", Int. J. Therm. Sci., vol. 91, pp. 113-124, 2015.

[31] C. Torrence, G. P. Compo, A Practical Guide to Wavelet Analysis. Bulletin of the American Meteorological Society, 79(1), 61-78, 1998